Cardanol Biomass-Derived Hard Carbon: A Promising Anode Material for Sodium-Ion Batteries

Weichen Li[1], Xiang Zheng[1], Luchao Yue[2], Zhi Wang[2], Chaohong Shi[1], and Jing Tang*[1, 3]

1. State Key Laboratory of Petroleum Molecular & Process Engineering, Shanghai Key Laboratory of Green Chemistry and Chemical Processes, School of Chemistry and Molecular Engineering, East China Normal University, Shanghai 200062, China.

2. School of Materials Science and Engineering, North University of China, Taiyuan, Shanxi, 030051, China.

3. Institute of Eco-Chongming, Shanghai 202162, China.

Email: jingtang@chem.ecnu.edu.cn

Material characterization

The morphology was observed by using scanning electron microscopy (Zeiss GeminiSEM450) and transmission electron microscopy (JEOL JEM-2100F). X-ray photoelectron spectroscopy (XPS, Kratos Ultra 2) was employed to investigated the surface compositions. X-ray diffraction (XRD) was operated with a scan rate of 2 ° min^{-1} by using the Rigaku Ultima IV XRD. The Bragg's equation (eq. S1)

$$2d \sin\theta = n\lambda \quad (1)$$

λ denotes the wavelength of Cu Kα radiation (1.5406 Å), used throughout this study.

θ is thereflection angle of peak (002).

The Scherrer equations for calculating Lc and La are as follows:

$$L_c = \frac{0.89\lambda}{\beta \cos\theta}$$

$$L_c = \frac{1.84\lambda}{\beta \cos\theta}$$

Raman spectra at 532 nm were obtained using a Thermo Fisher Scientific DXR2.

The specific surface area and pore parameters were determined using a nitrogen adsorption desorption apparatus (Micromeritics ASAP 2020 V4.01). The chemical structure and chemical bonds of the sample were measured by Fourier transform infrared absorption spectroscopy (Thermo Fisher Nicolet IS50).

Electrode preparation and electrochemical measurement

All the electrochemical testing was conducted in CR2032 coin cells, which were assembled in an argon-filled glove box (H_2O<0.01 ppm, O_2<0.01 ppm). The process for producing hard carbon anodes involved a mixture of hard carbon, Super-P, and carboxymethyl cellulose (CMC) binders, with a mass ratio of 7:2:1, in a slurry using deionized water as the dispersant. The active mass loading of each electrode was 1.8–2.2 mg cm^{-2}. 1.0 M NaPF6 in 1,2-Dimethoxyethane (DME) (1:1 in volume) was used as the electrolyte and glass fiber was performed as the separator. Cyclic voltammetry (CV) and electrochemical impedance spectroscopy (EIS) were conducted utilizing an

electrochemistry workstation (CHI 760e). The scan rates used for the CV test were 0.1, 0.2, 0.4, 0.6, 0.8, and 1 mV s^{-1}, covering a voltage range from 0.01 to 2 V. EIS was conducted with a frequency range from 100 kHz to 10 mHz. The galvanostatic charge/discharge (GCD) experiments were conducted using the Land battery test system. Current densities ranged from 0.05 to 1 A g^{-1}, with voltage ranges of 0.01–2 V. Galvanostatic Intermittent Titration Technique (GITT) tests were recorded on the Land battery test system in the voltage range of 0.01–2.00 V vs. Na^+/Na. The tests were performed at 0.1 A g^{-1} for 10 min, with a 60-minute relaxation period between each charge and discharge under constant-current conditions. For the full cell, GCD measurements were conducted at current densities of 0.1 A g^{-1} with a voltage range from 1.5 to 3.5 V.

The diffusivity coefficient of sodium ions (D_{Na^+}) can be calculated using Fick's second law:

$$D = \frac{4}{\pi\tau}\left(\frac{m_B V_M}{M_B S}\right)^2\left(\frac{\Delta E_S}{\Delta E_\tau}\right)^2 \quad (4)$$

Inside:
τ - the pulse duration (s)
m_B - the active mass of electrodes (g)
M_B - the molar mass of HC (g mol^{-1})
V_M - the molar volume (cm^3 mol^{-1})
S - the active surface area of the electrodes (cm^2)
ΔEs - the voltage difference during the rest intervals
$\Delta E\tau$ - the voltage difference during the current pulse

Ex-Situ Raman Spectroscopy Analysis

The electrode preparation and battery assembly followed the same procedures as outlined above. Galvanostatic charge-discharge tests were conducted using a Neware BTS-4008 battery testing system over the specified voltage range to obtain samples at various states—for example, charged to 0.01 V or discharged to 2.0 V. To retrieve the samples, batteries were disassembled in a glove box, and the hard carbon electrodes were removed, rinsed three times with DME to clear surface residual electrolyte,

vacuum-dried at 60 °C for 2 hours, and then sealed for storage to prevent contamination from atmospheric O_2 and H_2O.

For ex-situ Raman spectroscopy, a Thermo Scientific DXR2 confocal Raman spectrometer was used with a 532 nm laser, and the following parameters were set: a scanning range of 400–2000 cm^{-1} (covering the D band at 1350 cm^{-1} and G band at 1580 cm^{-1}), a laser power of 5–10 mW (to avoid structural damage from laser overheating), a resolution of 1–2 cm^{-1}, and 3–5 accumulations (to improve signal-to-noise ratio, SNR). During testing, the treated hard carbon electrode was mounted on the sample stage, and the laser was focused on the electrode surface while avoiding interference from the copper foil substrate to collect Raman spectra. Each sample was analyzed at three distinct regions, and the average was calculated to ensure repeatability.

Ex-Situ XRD Analysis

The sample preparation procedure is identical to that used for ex-situ Raman spectroscopy. Ex-situ XRD measurements were performed on the hard carbon material using a JEOL JEM-2100F high-resolution X-ray diffractometer. The radiation source was a Cu Kα line (λ=0.15406 nm), operating at a tube voltage of 35 kV and a tube current of 25 mA. The scanning range was typically set to 10°–60° (encompassing the characteristic diffraction peaks of hard carbon, including the (002) peak at 22° and (100) peak at 43°), with a scanning speed of 2° min^{-1}.

Table. S1 Preparation condition and corresponding structural parameters of all specimens appearing in this article.

Samples	d_{002} [nm] (XRD)	$V_{pore}(N_2)$ [$cm^3\ g^{-1}$]	I_D/I_G	S_{BET} [$m^2\ g^{-1}$]
Glu-450-1000	0.416744	0.5105	2.14	1151.1
Glu-CA-350-1000	0.41013	0.018805	2.33	4.9868
Glu-CA-450-1000	0.391579	0.036997	2.26	43.2445
Glu-CA-550-1000	0.385565	0.074261	2.07	103.3445

Table. S2 Preparation condition and corresponding electrochemical properties data of all specimens appearing in this article.

	ICE [%]	Slope capacity [$mAh\ g^{-1}$]	Plateau capacity [$mAh\ g^{-1}$]
Glu-450-1000	67.58	117	2
Glu-CA-350-1000	78.04	142	127
Glu-CA-450-1000	81.42	170	157
Glu-CA-550-1000	73.14	160	100

Below is a table that presents a systematic comparison of the electrochemical behaviors between advanced hard carbon materials and other biomass-derived carbon materials reported recently.

Table S3. Comparison of the ICE and specific capacity of hard carbon anodes.

	ICE [%]	**Reversible capacity (mAh g^{-1})/ current densities (mA g^{-1})**	**Reference**
Glu-CA-450-1000	86	365.8 (100)	This Work
CCD-1300	91	300 (20)	[S1]
CEM-G-8h	89	310 (30)	[S2]
FP-MP 5:2 1000	80	282 (30)	[S3]
HC-N	88	356 (20)	[S4]
PCBC125	89	330 (20)	[S5]
CS-1200	91	337 (20)	[S6]
MCC1400	81	343 (30)	[S7]
HC/SC	85	314 (30)	[S8]
SDR14	84	295 (100)	[S9]

Table S4. Comparison of performance of biomass hard carbon.

	ICE [%]	**Reversible capacity (mAh g-1)/ current densities (mA g-1)**	**Reference**
Starch	85	260 (30)	[S10]
Lignin	63	292 (100)	[S11]
Nut shells	84	298 (100)	[S12]
Cotton	75	272 (50)	[S13]
Wool	63	303 (63)	[S14]
Tea	69	282 (30)	[S15]

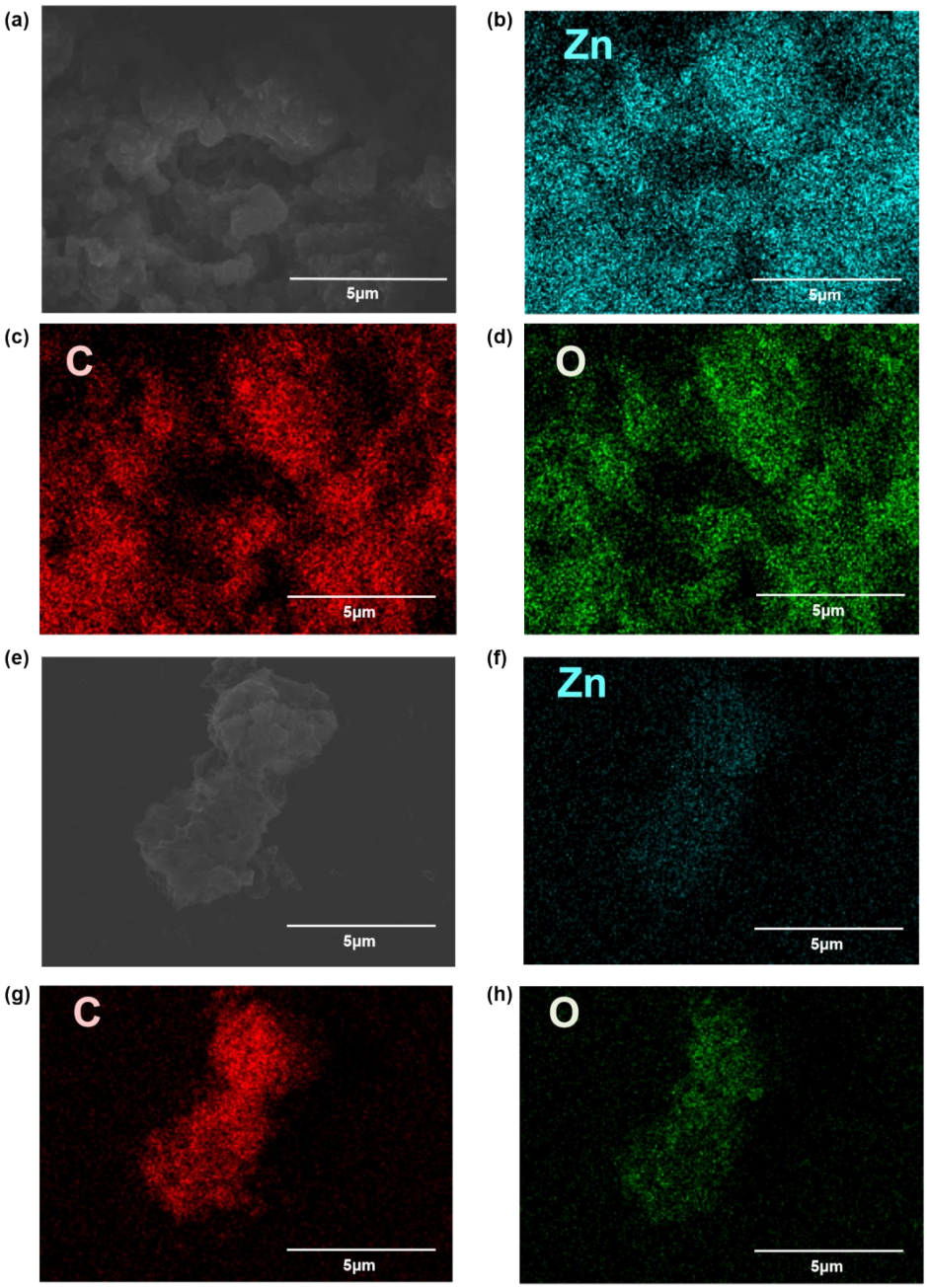

Figure S1. SEM image and corresponding EDS mappings of Glu-CA-450 before (a-d) and after (e-h) acid etching.

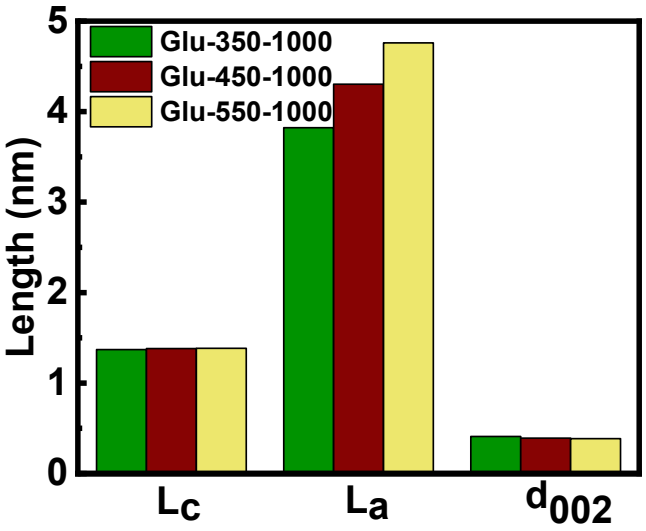

Figure S2. L_c, L_a, d_{002} of Glu-CA-x-1000 (x = 350, 450, 550)

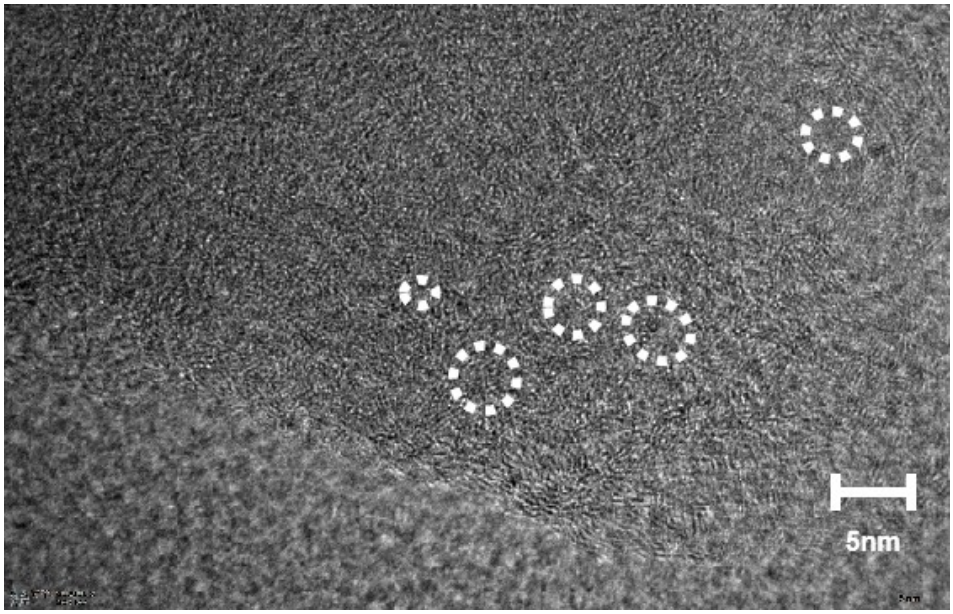

Figure S3. TEM images of Glu-CA-350-1000.

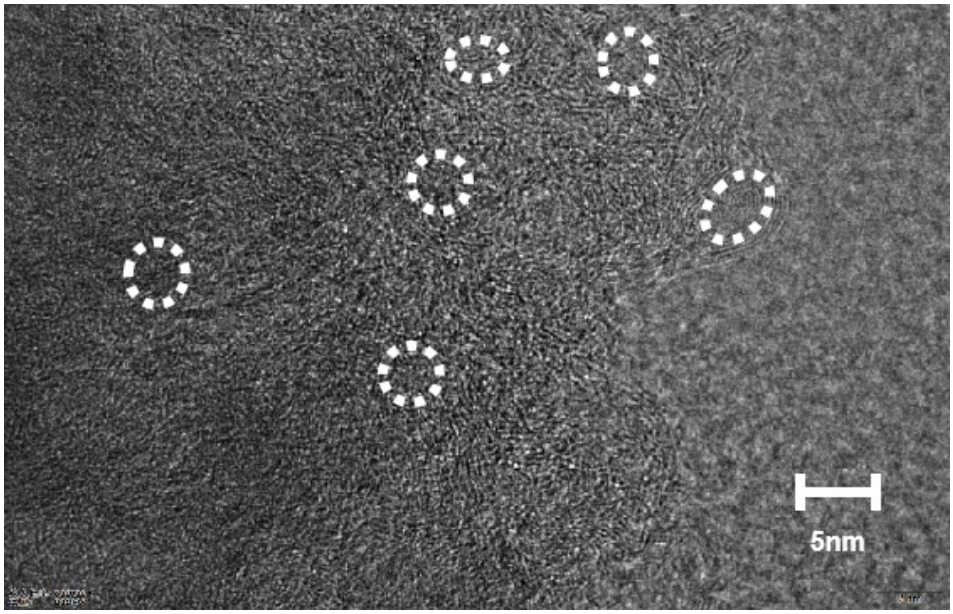

Figure S4. TEM images of Glu-CA-450-1000.

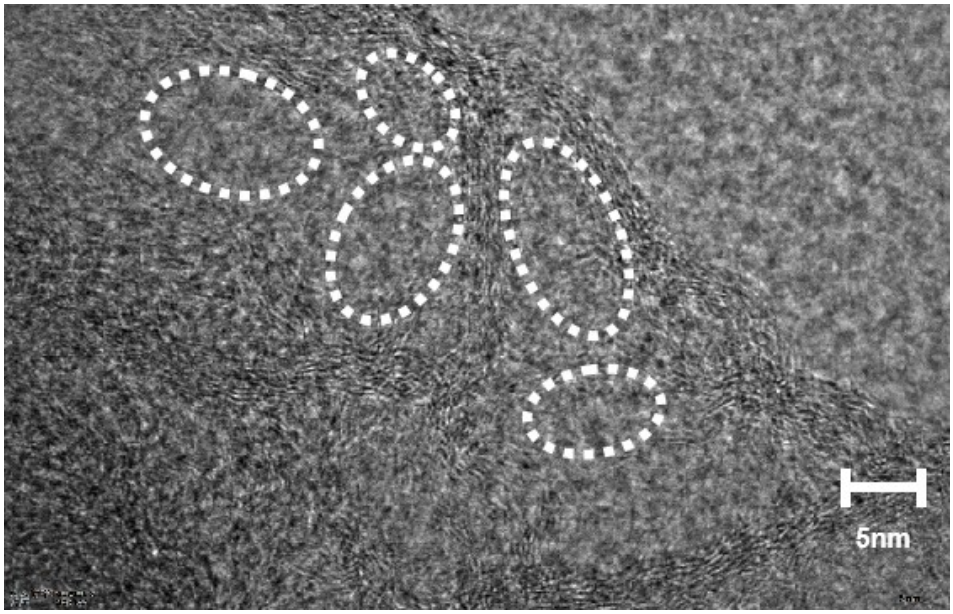

Figure S5. TEM images of Glu-CA-550-1000.

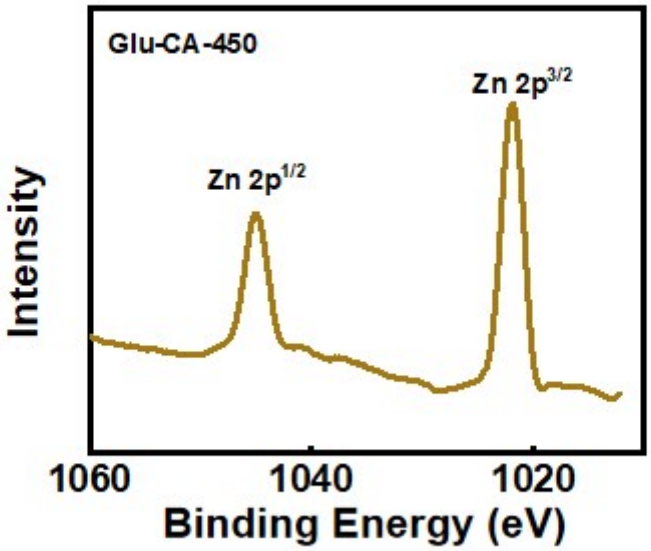

Figure S6. High-resolution Zn 2p spectra of Glu-CA-450.

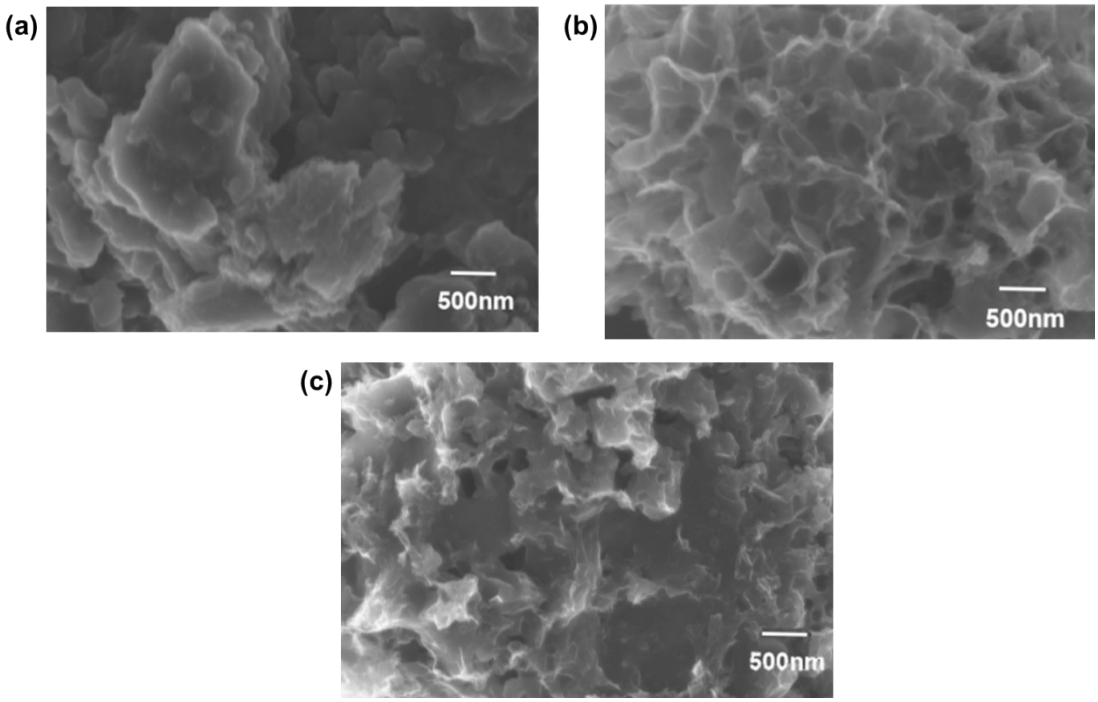

Figure S7. SEM images of (a) Glu-450-1000 (b) CA-1000 (c) Glu-CA-450-1000.

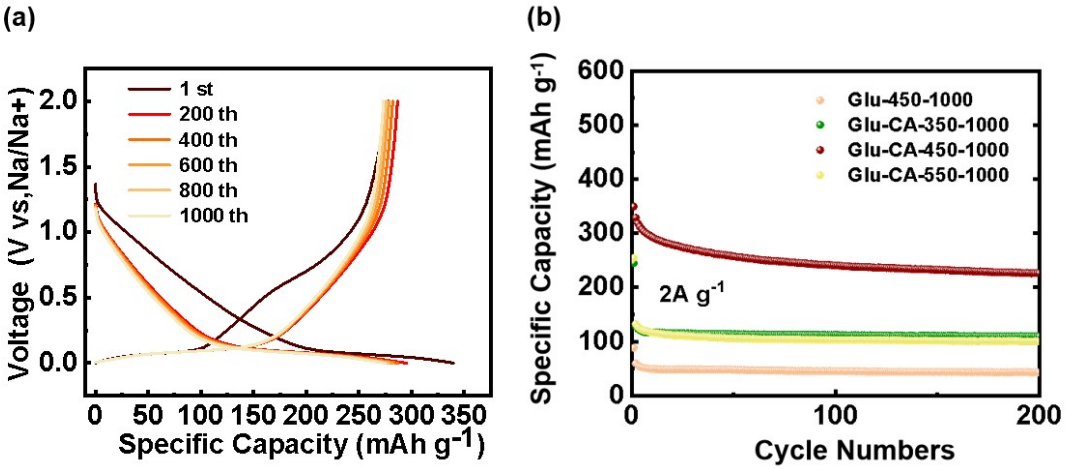

Figure S8. (a) Charge/discharge curves illustrating the cycling performance of the samples (b) Cycling performance of Glu-450-1000 and Glu-CA-*x*-1000 at 2A g^{-1}.

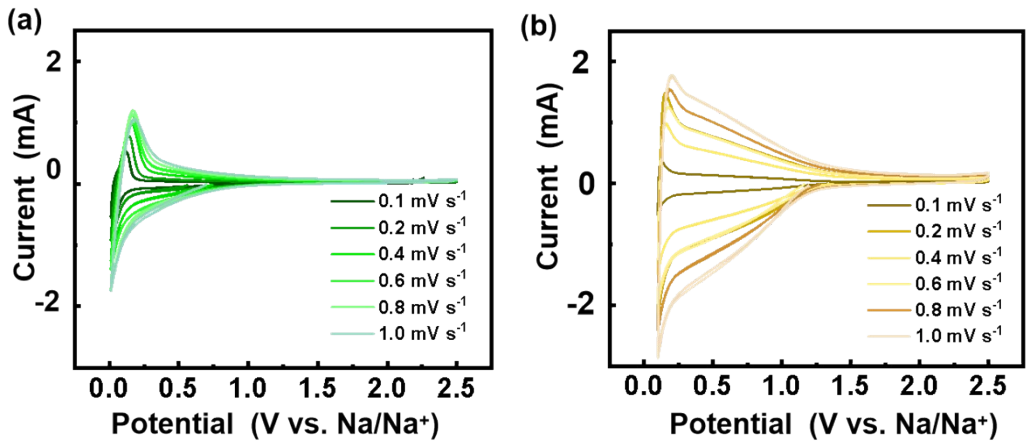

Figure S9. (a) CV curves of Glu-CA-350-1000. (b) CV curves of Glu-CA-550-1000.

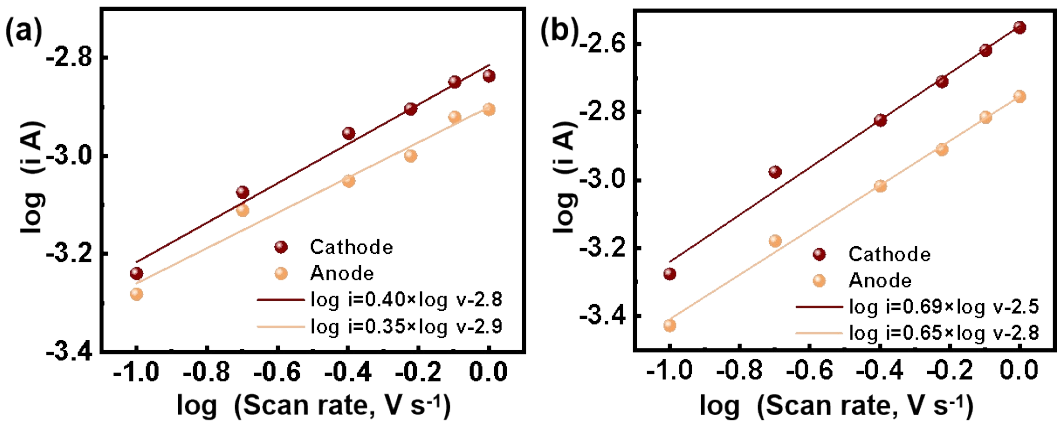

Figure S10. (a) Glu-CA-350-1000 plots of log (sweep rate) versus log (current). (b) Glu-CA-550-1000 plots of log (sweep rate) versus log (current).

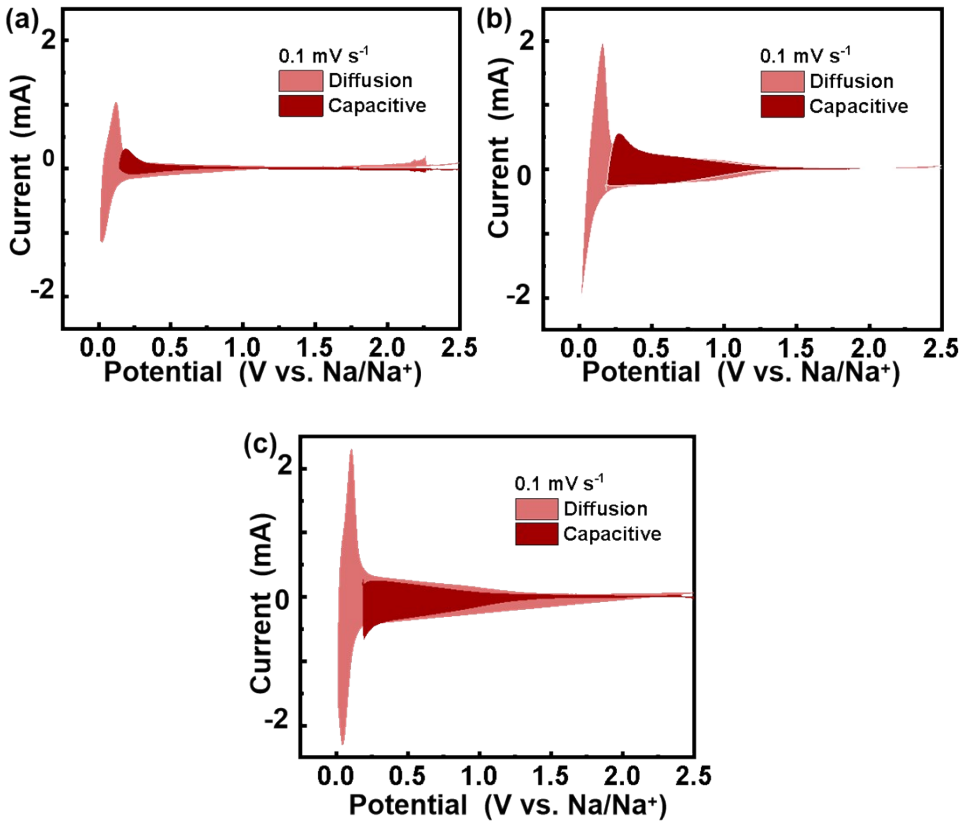

Figure S11. (a) Schematic diagrams of pseudocapacitive contribution of Glu-CA-350-1000 at a scan rate of 0.1 mV s^{-1}. (b) Schematic diagrams of pseudocapacitive contribution of Glu-CA-450-1000 at a scan rate of 0.1 mV s^{-1}. (c) Schematic diagrams of pseudocapacitive contribution of Glu-CA-550-1000 at a scan rate of 0.1 mV s^{-1}.

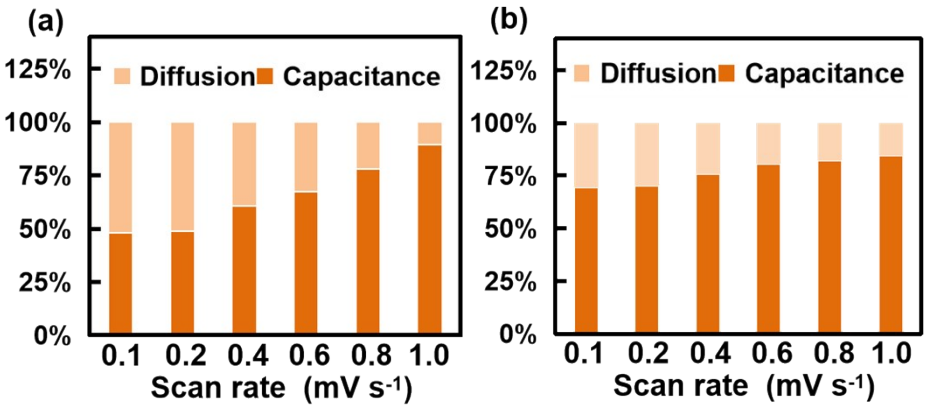

Figure S12. (a) Contribution of diffusion- and capacitive-controlled capacity of Glu-CA-350-1000. (b) Contribution of diffusion- and capacitive-controlled capacity of Glu-CA-550-1000.

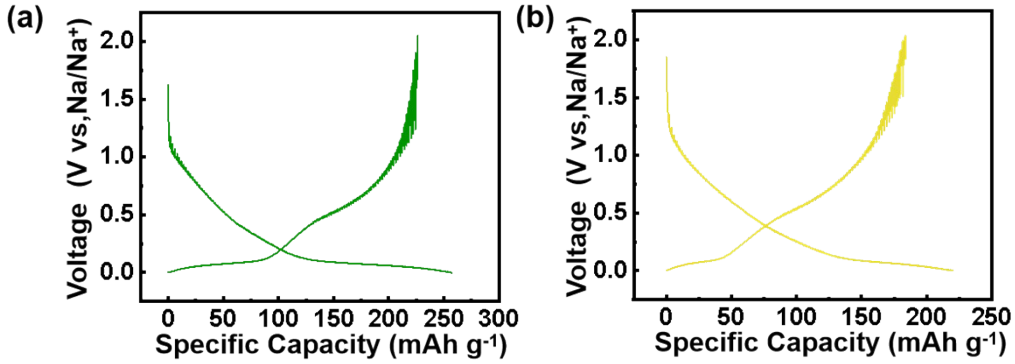

Figure S13. (a) GITT curves of Glu-CA-350-1000 at the third cycle. (b) GITT curves of Glu-CA-550-1000 at the third cycle.

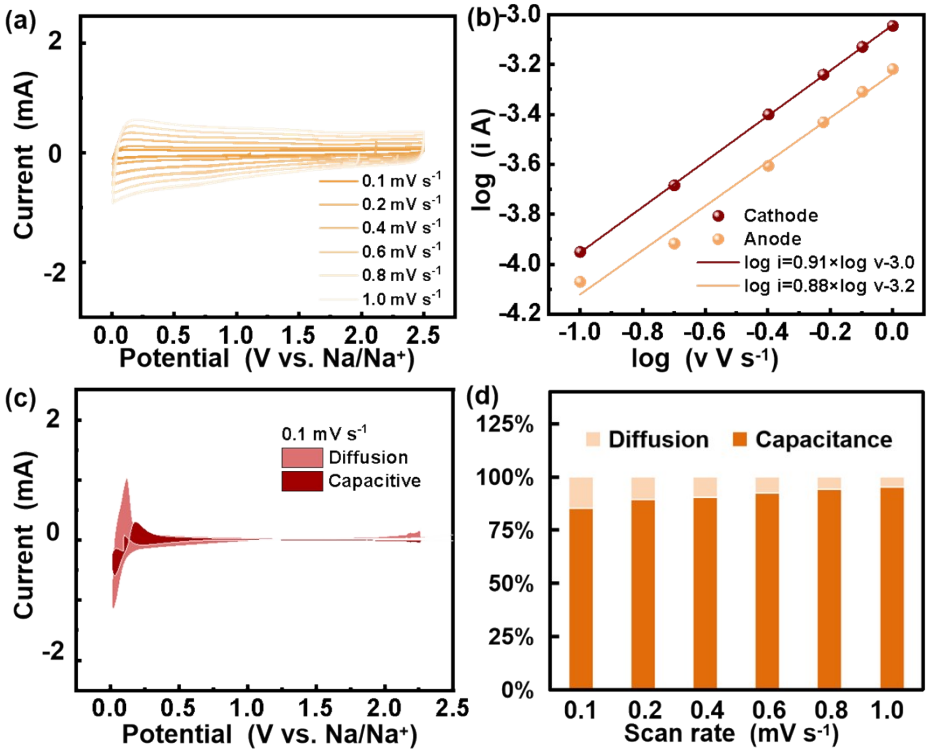

Figure S14. (a) CV curves of Glu-450-1000. (b) Schematic diagrams of pseudocapacitive contribution of Glu-450-1000 at a scan rate of 0.1 mV s^{-1}. (c) Glu-450-1000 plots of log (sweep rate) versus log (current). (d) Contribution of diffusion- and capacitive-controlled capacity of Glu-450-1000.

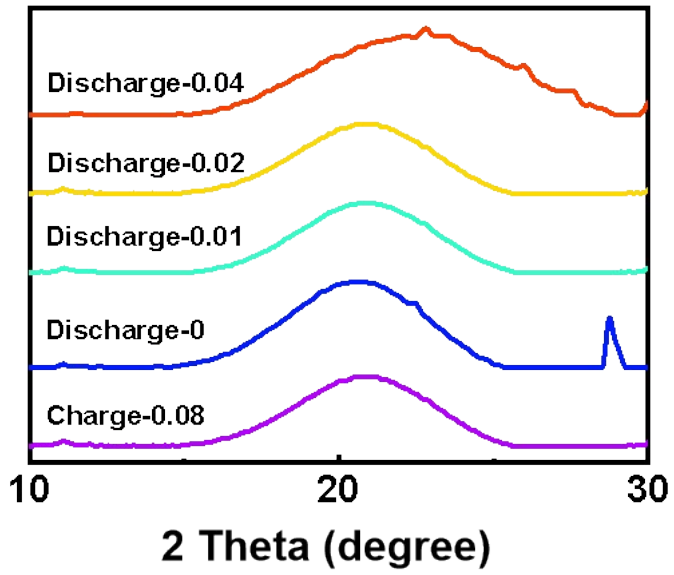

Figure S15. Ex-situ XRD during the initial cycles of Glu-CA-450-1000.

References

[S1] F. Xie, Z. Xu, A. C. S. Jensen, F. X. Ding, H. Au, J. Y. Feng, H. Luo, M. Qiao, Z. Y. Guo, Y. X. Lu, A. J. Drew, Y. S. Hu, M. M. Titirici. J Mater Chem A., 2019, 7, 27567.

[S2] X. Zhao, Y. Ding, Q. Xu, X. Yu, Y. Liu, H. Shen. Adv Energy Mater., 2019, 9, 1803648.

[S3] F. Xie, Z. Xu, A. C. S. Jensen, H. Au, Y. X. Lu, V. Araullo-Peters, A. J. Drew, Y. S. Hu, M. M. Titirici. Adv Funct Mater., 2019, 29, 1901072.

[S4] Y. Huang, Z. Hou, J. Wang, Y. Li, T. Ma, D. Nan, C. Wei, J. Wang. Angew. Chem. Int. Ed., 2025, 64, e202423864.

[S5] G. Zhao, T. Xu, Y. Zhao, Z. Yi, L. Xie, F. Su, Z. Yao, X. Zhao, J. Zhang, W. Xie, X. Li, L. Dong, C.-M. Chen. Energy Storage Mater., 2024, 67, 103282.

[S6] M. Li, Y. Wang, Y. Zhang, N. Zhang. Molecular Tailoring of Biomass Precursor to Regulate Hard Carbon Microstructure for Sodium Ion Batteries. Chem. Eng. J., 2025, 506, 160083.

[S7] D. Li, C. Gao, X. He, Y. Gao, L. Wang, C. Jia, Y. Zhang. Waste Asphalt-Derived Hard Carbon Assisted by Biomass Templating for Sodium-Ion Batteries. Chem. Eng. J., 2025, 522, 167350.

[S8] J. Cui, W. Li, P. Su, X. Song, W. Ye, Y. Zhang, Z. Chen. Adv. Energy Mater., 2025, 15, 2502082.

[S9] H.-W. Chi, J.-Y. Chen, C.-C. Yang, W.-R. Liu. Carbon. 2026, 246, 120899.

[S10] Y.K. Sun, T.C. Shen, H.L. Pan, Z.J. He, B. Ru, G.X. Dai, S.R. Wang. Regulating the Microstructure of Cross-Linked Starch-Derived Hard Carbon for Highly Reversible Sodium-Ion Storage. Appl. Surf. Sci., 2025, 680, 161422.

[S11] A. Wang, G.Y. Zhang, M. Li, Y.T. Sun, Y.W. Tang, K. Sun, J.M. Lee, G.T. Fu, J.C. Jiang. Lignin Derived Hard Carbon for Sodium Ion Batteries: Recent Advances and Future Perspectives. Prog. Mater. Sci., 152 (2025), Article 101452.

[S12] H. Guo, K. Sun, Y.X. Lu, H.L. Wang, X.B. Ma, Z.Y. Li, Y.S. Hu, D.F. Chen. Hard Carbons Derived from Pine Nut Shells as Anode Materials for Na-Ion Batteries Chin. Phys. B., 2019, 28, 068203.

[S13] H.R. Sarma, J. Sun, Y. Hora, M. Forsyth, N. Byrne. Effect of Carbonization Behaviour of Cotton Biomass in Electrodes for Sodium-Ion Batteries. ChemElectroChem, 2023, 10, e202300281.

[S14] X.M. Zhu, Q. Li, S. Qiu, X.L. Liu, L.F. Xiao, X.P. Ai, H.X. Yang, Y.L. Cao. Hard Carbon Fibers Pyrolyzed from Wool as High-Performance Anode for Sodium-Ion Batteries. JOM, 2016, 68, 2579-2584.

[S15] L.Y. Pei, H.L. Cao, L.T. Yang, P.Z. Liu, M. Zhao, B.S. Xu, J.J. Guo. Hard Carbon Derived from Waste Tea Biomass as High-Performance Anode Material for Sodium-Ion Batteries. Ionics, 2020, 26, 5535-5542.